CrystEngComm

ROYAL SOCIETY OF CHEMISTRY

PAPER

View Article Online
View Journal | View Issue

Cite this: *CrystEngComm*, 2025, **27**, 7677

Versatility of the methyl-bipyrimidine-*N*-oxide ligand for the design of lanthanide single-molecule magnets

Haiet Douib,[ab] Bertrand Lefeuvre,[a] Jessica Flores Gonzalez,[a] Vincent Dorcet[a] and Fabrice Pointillart *[a]

Received 26th August 2025,
Accepted 13th October 2025

DOI: 10.1039/d5ce00831j

rsc.li/crystengcomm

A library of ten complexes, $[Yb_2(hfac)_6(L)]$ (**1**), $[Yb_6(hfac)_{14}(OH)_4(L)_2]$ (**2**), $[Dy(hfac)_3(L)]_2{\cdot}C_2H_4Cl_2$ ((**3**)$\cdot C_2H_4Cl_2$), $[Dy(hfac)_3(L)]_2[Dy(hfac)_3(H_2O)_2]$ (**4**), $[Dy_6(hfac)_{14}(OH)_4(L)_2]$ (**5**), $[Yb(tta)_3(L)]$ (**6**) and $[Ln_2(hfc)_6(L)]$ (Ln = Dy ((–)**7**, (+)**7**) and Yb ((–)**8**, (+)**8**)) (where $hfac^-$ = 1,1,1,5,5,5-hexafluoroacetylacetonate, tta^- = 2-thenoyltrifluoroacetylacetonate, hfc^- = 3-(heptafluoropropylhydroxymethylene-(±)-camphorate and L = 4-methylbipyrimidine-2-*N*-oxide ligand)) were isolated and characterized by single crystal and powder X-ray diffraction. All the Yb(III) based-complexes demonstrate a slow relaxation of the magnetization under an applied DC field, which occurs through a Raman process and an additional Orbach process for **6**. The two Dy(III) dinuclear complexes **3** and (±)**7** display slow magnetic relaxation in a zero applied DC field, whereas complex **4**, which is similar to **3** with co-crystallization of $Dy(hfac)_3(H_2O)_2$, presents only a field-induced slow magnetic relaxation. Multi-field-induced single-molecule magnet (SMM) behaviour was observed for (+)**7**, while this was not the case for the Yb(III) analogue (+)**8**.

Introduction

Coordination chemistry and lanthanide ions have been the key ingredients for designing molecular systems which display slow magnetic relaxation, called single-molecule magnets (SMM), since the discovery of such magnetic behaviour for a mononuclear complex of terbium in 2003.[1] On the one hand, the high magnetic moment and strong magnetic anisotropy of lanthanides make them suitable candidates to obtain SMMs. On the other hand, coordination chemistry allows the imposition of an appropriate axial crystal field to induce axial magnetic anisotropy in the ground state, which is required for anisotropic oblate-shaped 4f electron density like for the Dy(III) ion.[2] Such a synthetic approach led to the observation of a high blocking temperature (T_B)[3–13] up to 100 K (ref. 14) for lanthanide organometallic complexes. It is worth noting that other synthetic strategies have been explored to improve SMM performances through the elimination of the fast magnetic relaxation through quantum tunneling of the magnetization (QTM) by imposing strong magnetic interaction in π–4f systems (where π electrons come from organic radical ligands)[15,16] or mixed-valence lanthanide complexes with metal–metal bonding.[9] Such enthusiasm for 25 years towards lanthanide SMMs is motivated by the potential applications in high-density data storage,[17] quantum computing[18] and spintronics[19] offered by such molecular systems. One specific ligand family that can be used to design SMMs is the pyridine-*N*-oxide derivatives.[20–25] In particular, our group demonstrated that such ligands lead to the formation of mononuclear,[26,27] dinuclear[28–31] and tetranuclear[32] species due to the terminal or bridging mode of coordination of the nitroxide group. Moreover, the pyridine-*N*-oxide moiety can be involved in the synthesis of ditopic ligands to achieve the elaboration of homo-bimetallic 4f systems, and heterobimetallic 3d4f and 4f4f′ systems to observe multi-SMM behaviour.[33–35] An easy way to control the final molecular architecture of the complexes is to start from the Ln(β-diketonate)$_3(H_2O)_n$ (n = 1–3) units.[36] In this context, E. Colacio and co. designed the 4-methylbipyrimidine-2-*N*-oxide ligand (L), proposing two different bischelating coordination sites (Scheme 1), which in the presence of Dy(β-diketonate)$_3(H_2O)_2$ (where β-diketonate = $hfac^-$ = 1,1,1,5,5,5-hexafluoroacetylacetonate) led to the formation of a binuclear SMM with the two Dy(III) displaying slow magnetic relaxation at different rates.[37] Finally, multifunctional SMMs could be isolated using chiral β-diketonate as the combination of chirality and magnetism leads to the appearance of ferroelectricity[38] and magneto-chiral dichroism (MChD),[39] as observed by some of us in lanthanide coordination complexes.[40]

[a] *Univ Rennes, CNRS, ISCR (Institut des Sciences Chimiques de Rennes) – UMR 6226, 35000 Rennes, France. E-mail: fabrice.pointillart@univ-rennes.fr*
[b] *Laboratoire des Matériaux Organiques et Hétérochimie (LMOH), Département des Sciences de la Matière, Université Larbi, Tébessi de Tébessa, Tébessa, Algéria*

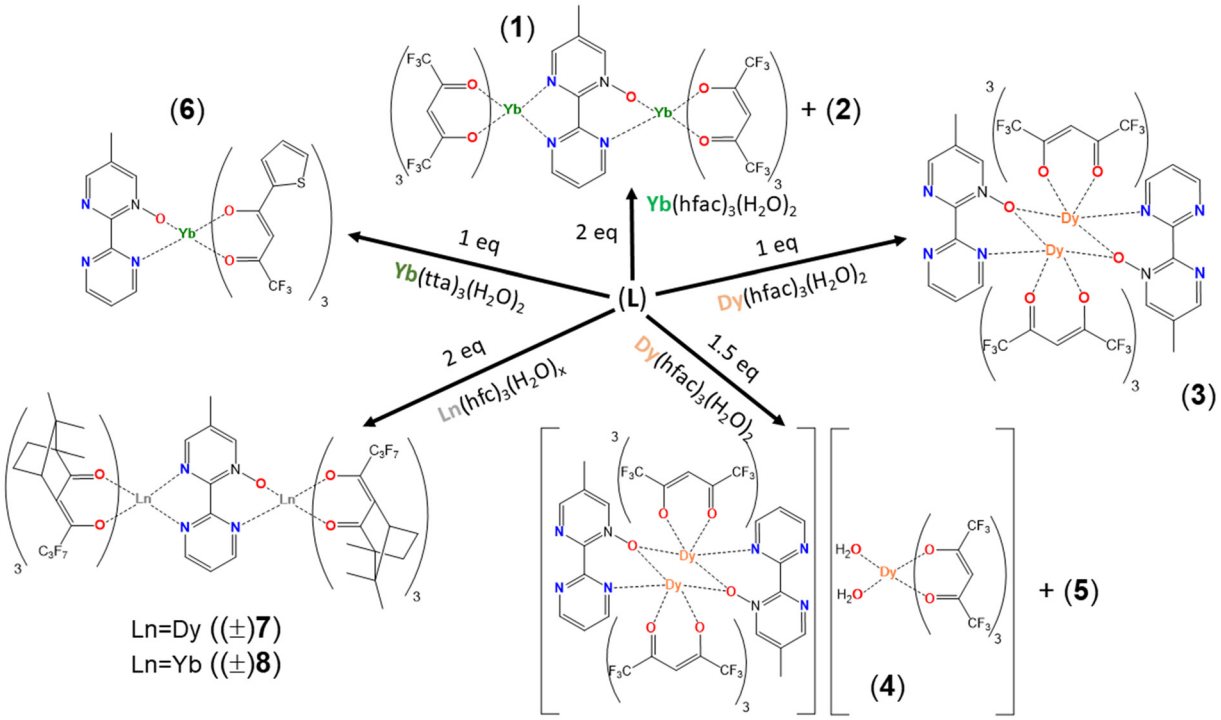

Scheme 1 Synthetic routes to obtain complexes **1**–**8**.

In this paper, we propose to extend the possibility of coordination offered by the L ligand in the presence of Ln(β-diketonate)$_3$(H$_2$O)$_n$ (n = 1–2, Ln = Dy(III) and Yb(III) and β-diketonate = 1,1,1,5,5,5-hexafluoroacetylacetonate (hfac$^-$)), 2-tenoyltrifluoroacetylacetonate (tta$^-$) and 3-(heptafluoropropylhydroxymethylene-(±)-camphorate (hfc$^-$)) with different Ln : L ratios. Mononuclear, dinuclear, trinuclear and hexanuclear complexes have been isolated and characterized by single crystal and powder X-ray diffraction, while their magnetic and chiroptical properties have been investigated by DC and AC magnetic measurement, absorption spectroscopy and natural circular dichroism.

Results and discussion

Synthesis

The library of coordination lanthanide complexes involving the 4-methylbipyrimidine-2-*N*-oxide (**L**) ligand[37] was obtained by mixing different Ln(β-diketonate)$_3$(H$_2$O)$_n$ metallo-precursors (Ln(III) = Dy and Yb, n = 1 or 2 and β-diketonate = 1,1,1,5,5,5-hexafluoroacetylacetonate (hfac$^-$)), 2-thenoyltrifluoroacetylacetonate (tta$^-$) and 3-(heptafluoropropylhydroxymethylene-(±)-camphorate (hfc$^-$)). The nature of the final complex depends on two criteria, which are i) the ratio between the metallo-precursor and L and ii) the nature/bulkiness of the β-diketonate anion (Scheme 1). For a ratio (Ln : L) of 2, a dinuclear complex was isolated in which the two N–N and O–N bischelating sites of coordination are occupied (complexes **1**, (−)**7**/(+)**7** and (−)**8**/(+)**8**). For a ratio of 1 (Ln : L), only the O–N bischelating site of coordination is occupied, while the N–N bischelating site of coordination remains free due to the oxophilic character of the lanthanide ions. When the Ln(tta)$_3$(H$_2$O)$_2$ (Ln = Dy and Yb) species are used, mononuclear complexes are isolated (complex **6**),[37] while using Dy(hfac)$_3$(H$_2$O)$_2$ resulted in a dinuclear complex (complex **3**). The difference in the synthetic behaviour could be explained by the difference in the steric hindrance between the two tta$^-$ and hfac$^-$ ancillary ligands. Finally, a ratio of 1.5 (Dy : L) led to the formation of dinuclear complex **4** with the co-crystallization of Dy(hfac)$_3$(H$_2$O)$_2$. Notably, during the synthesis of **1** and **4**, single crystals of hexanuclear complexes **2** and **5** were isolated as a very minor fraction.

Crystal structure analysis

[Yb$_2$(hfac)$_6$(L)] (1). [Yb$_2$(hfac)$_6$(L)] (**1**) crystallizes in the triclinic $P\bar{1}$ space group (Table S1), and its asymmetric unit is

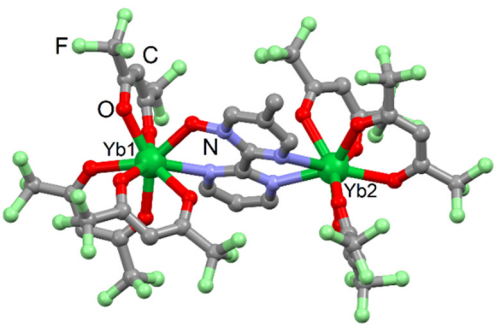

Fig. 1 Molecular structure of [Yb$_2$(hfac)$_6$(L)] (**1**) determined from single crystal X-ray diffraction. Hydrogen atoms are omitted for clarity. Dark green, Yb; green, F; red, O; blue, N; and gray, C.

composed of a binuclear complex (Fig. 1) of formula $[Yb_2(hfac)_6(L)]$. The ligand L bridges two Yb(III) ions through its two N–N and N–O coordination sites, leading to an O7N coordination sphere around Yb1, while Yb2 adopted an O8 environment. The average Yb1–O, Yb2–O, Yb1–N and Yb2–N distances are 2.284(6) Å, 2.541(6) Å, 2.281(6) Å and 2.491(6) Å, respectively. The coordination environment adopted a triangular dodecahedron geometry (D_{2d} symmetry) with a less pronounced distortion for Yb1 (CShM(D_{2d}) 0.472) than for Yb2 (CShM(D_{2d}) 1.144) (Table S2).

The distortion was visualized by continuous shape measurements performed with SHAPE 2.1.[41] The torsion angle defined by the angle made by the planes involving the two pyrazine rings was calculated to be 11.7(2)°. The coordination of the nitrogenated chelating site imposes limited torsion between the pyrazine moieties. The intramolecular Yb–Yb distance is 6.818(3) Å. The crystal packing revealed that the cohesion of the structure takes place through H···F and F···F short contacts. The shortest intermolecular Yb–Yb distance is 6.834(3) Å. The phase purity of **1** was confirmed by powder X-ray diffraction investigation (Fig. S1).

$[Yb_6(hfac)_{14}(OH)_4(L)_2]$ (2) and $[Dy_6(hfac)_{14}(OH)_4(L)_2]$ (5). **2** and **5** have very similar molecular structures even if **2** crystallizes in the monoclinic $P2_1/c$ space group (Table S1), while **5** (Fig. S2) crystallizes in the monoclinic $P2_1/n$ space group with different cell parameters (Table S1). Thus, only the structural analysis for **2** is given in the following details. The ligand L coordinates an Yb(hfac)$_3$ unit through its nitrogenated bischelating site, leading to a N2O6 coordination sphere around these two Yb(III) ions with average Yb–O and Yb–N bond lengths of 2.260(11) Å and 2.493(13) Å. Such terminal ions adopt a square antiprism coordination geometry (CShM(D_{4d}) 0.636) for Yb5 and 0.487 for Yb6 (Table S2). The N–O coordination site coordinates two other Yb(III) centers through the μ_2 bridging nitroxide group. The four Yb(III) ions (Yb1, Yb2, Yb3 and Yb4) coordinate to the nitroxide group to form a distorted cubane for which the heights are occupied by four Yb(hfac)$_2$ moieties and by four μ_3 bridging OH^- hydroxy groups (Fig. 2). Moreover, two of the cubane faces are capped by the two N–O groups. Surprisingly, despite a similar environment around the four Yb(III) metal ions composing the cubane, Yb1 and Yb3 adopt a distorted square antiprism (CShM(D_{4d}) 1.015 for Yb1 and 1.302 for Yb2) (Table S2), while Yb2 and Yb4 adopt a distorted triangular dodecahedron (CShM(D_{2d}) 1.167 for Yb2 and 1.715 for Yb4) (Table S2). Finally, a hexanuclear complex was identified. The torsion angle was calculated to be 17.0(3)°.

The Yb(III) ions bridged by three oxygen atoms generate the shortest intramolecular Yb–Yb distances of 3.476(3) Å (Yb1···Yb4) and 3.481(3) Å (Yb2···Yb3). When the Yb(III) species are bridged by two oxygen atoms, the resulting Yb–Yb distances are slightly longer (Yb1···Yb3 = 3.748(4) Å and Yb2···Yb4 = 3.767(4) Å). The intramolecular distance between the two-terminal N2O6 Yb(III) ions has been measured to be equal to 16.379(5) Å. The shortest intermolecular Yb–Yb distance is 8.818(4) Å between the Yb5 centres. As observed for **1**, the interactions between neighbouring hexanuclear complexes take place through H···F and F···F short contacts. The binuclear complex (Fig. 3) is generated by the inversion centre. To form (**3**)·$C_2H_4Cl_2$ only the N–O bischelating site is linked to the Dy(III) ion with the nitroxide group, which is bridging two metal centers. It is worth noting that the closest symmetries and coordination polyhedra around the Dy(III) ions in **5** are different from those in **2**. The two-terminal Dy5 and Dy6 ions adopt a triangular dodecahedron, while the four Dy(III) ions involved in the cubane adopt square antiprism (for Dy2 and Dy4) or intermediate geometries (for Dy1 and Dy3) (Table S2).

$[Dy(hfac)_3(L)]_2{\cdot}C_2H_4Cl_2$ ((3)·$C_2H_4Cl_2$). $[Dy(hfac)_3(L)]_2{\cdot}C_2H_4Cl_2$ ((**3**)·$C_2H_4Cl_2$) crystallizes in the monoclinic $P2_1/n$ space group (Table S1), and its asymmetric unit is composed of a one half $[Dy(hfac)_3(L)]_2{\cdot}C_2H_4Cl_2$ complex. The Dy(III) adopts an O8N environment with a Dy–O average bond length of 2.397(5) Å, which is shorter than the Dy–N (2.599(6) Å) leading to a spherical capped square antiprism coordination geometry (CShM(C_{4v}) 0.639) (Table S2). The torsion angle was calculated to be 29.9(2)°, which is higher than the one found

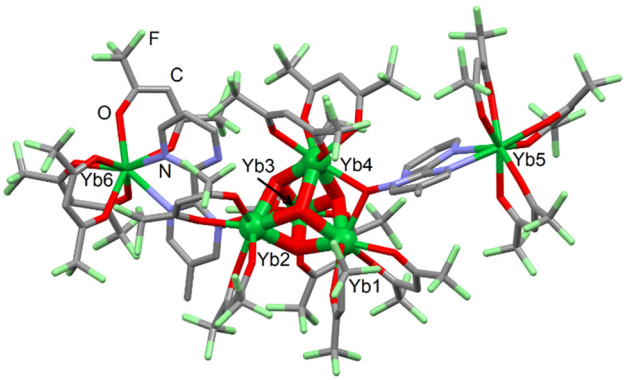

Fig. 2 Molecular structure of $[Yb_6(hfac)_{14}(OH)_4(L)_2]$ (**2**) determined from single crystal X-ray diffraction. Hydrogen atoms are omitted for clarity. Dark green, Yb; green, F; red, O; blue, N; and gray, C.

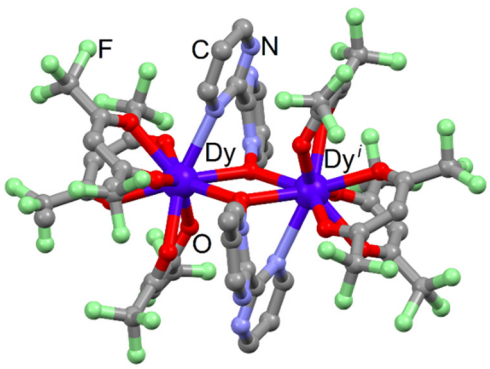

Fig. 3 Molecular structure of $[Dy(hfac)_3(L)]_2{\cdot}C_2H_4Cl_2$ (**3**)·$C_2H_4Cl_2$ determined from single crystal X-ray diffraction. Hydrogen atoms are omitted for clarity. Dark blue, Dy; green, F; red, O; blue, N; and gray, C.

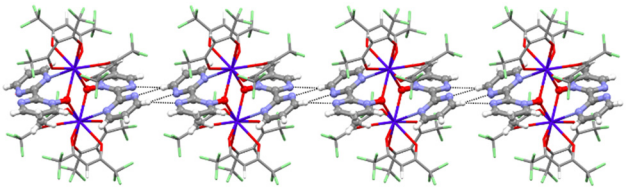

Fig. 4 Crystal packing of $[Dy(hfac)_3(L)]_2{\cdot}C_2H_4Cl_2$ (**3**)$\cdot C_2H_4Cl_2$ highlighting the short contacts between neighboring L ligands.

in **1** and **2** because the N–N coordination site remains free. The intramolecular Dy–Dy distance is 4.237(3) Å.

The crystal packing revealed that the cohesion of the structure takes place through short N···H contacts between two neighbouring L ligands (Fig. 4). Additional H···F and F···F short contacts have also been identified. The shortest intermolecular Dy–Dy distance is 10.998(4) Å. The phase purity of (**3**)$\cdot C_2H_4Cl_2$ was confirmed by powder X-ray diffraction investigation (Fig. S3).

$[Dy(hfac)_3(L)]_2[Dy(hfac)_3(H_2O)_2]$ (4). $[Dy(hfac)_3(L)]_2[Dy(hfac)_3(H_2O)_2]$ (**4**) crystallizes in the monoclinic *C*2/*c* space group (Table S1), and its asymmetric unit is composed of a one half $[Dy(hfac)_3(L)]_2$ and one half $Dy(hfac)_3(H_2O)_2$ complexes. The binuclear complex $[Dy(hfac)_3(L)]_2$ is very similar to the one described in the X-ray structure of **3**. The Dy(III) centre adopts a NO8 coordination sphere with the average Dy–O equal to 2.393(6) Å and Dy–N equal to 2.629(6) Å, with the two bridging ligands making a torsion angle of 30.5(3)° and leading to an intramolecular Dy–Dy distance of 4.224(3) Å. The Dy1 adopts the same spherical capped square antiprism coordination sphere to the Dy1 in (**3**)$\cdot(C_2H_4Cl_2)$ with a similar distortion degree (CShM(C_{4v}) 0.899) (Table S2). The main difference between the molecular structures of **3** and **4** lies in the co-crystallization of the $Dy(hfac)_3(H_2O)_2$ complex in the case of **4** (Fig. 5). In such a mononuclear complex, the Dy2 centre is surrounded by eight oxygen atoms coming from three deprotonated $hfac^-$ anions and two water molecules with an average Dy–O distance of 2.345(6) Å leading to a quasi-regular square antiprism (CShM(D_{4d}) 0.208) (Table S2).

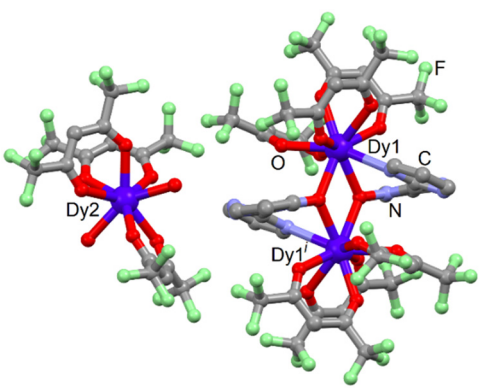

Fig. 5 Molecular structure of $[Dy(hfac)_3(L)]_2[Dy(hfac)_3(H_2O)_2]$ (**4**) determined from single crystal X-ray diffraction. Hydrogen atoms are omitted for clarity. Dark blue, Dy; green, F; red, O; blue, N; and gray, C.

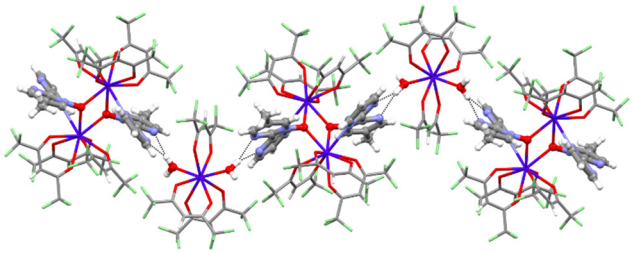

Fig. 6 Crystal packing of $[Dy(hfac)_3(L)]_2[Dy(hfac)_3(H_2O)_2]$ (**4**) highlighting the hydrogen bonds between neighboring mononuclear $[Dy(hfac)_3(H_2O)_2]$ and dinuclear $[Dy(hfac)_3(L)]_2$ complexes.

The crystal packing revealed that the complex plays a crucial role in the stabilization of the structure through the formation of hydrogen bonds between the water molecules and the remaining free N–N coordination site of L ($O34_w\cdots N2$ = 2.869(4) Å) (Fig. 6). A pseudo-one-dimensional polymer with alternating binuclear and mononuclear complexes is formed (Fig. 6). The shortest intermolecular Dy–Dy distance is 8.865(4) Å. The phase purity of **4** was confirmed by powder X-ray diffraction investigation (Fig. S4).

$[Yb(tta)_3(L)]$ (6). The Dy(III) analogue of **6** was previously reported.[37] **6** crystallizes in the orthorhombic *Pbcn* space group (Table S1), and its asymmetric unit is composed of one $[Yb(tta)_3(L)]$ complex (Fig. 7). The Yb(III) centre adopts a NO7 coordination sphere with the average Yb–O equal to 2.291(6) Å and Yb–N equal to 2.649(8) Å. The resulting coordination environment is a square antiprism (CShM(D_{4d}) 0.753) (Table S2). The torsion angle reached a value of 45.7(4)°, higher than the values observed for the previous complexes, because of the terminal bischelating mode of coordination of L in **6**. The crystal packing shows π–π stacking between the pyrazine and thiophene rings (Fig. 8). The shortest intermolecular Yb–Yb distance is 9.132(5) Å. The phase purity of **6** was confirmed by powder X-ray diffraction investigation (Fig. S5).

$[Ln_2(hfc)_6(L)]$ (Ln = Dy ((−)7, (+)7) and Yb ((−)8, (+)8)). Both Dy(III) and Yb(III) are isostructural, thus only the structure

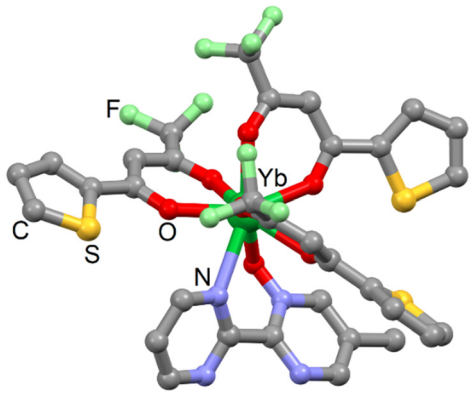

Fig. 7 Molecular structure of $[Yb(tta)_3(L)]$ (**6**) determined from single crystal X-ray diffraction. Hydrogen atoms are omitted for clarity. Dark green, Yb; green, F; red, O; blue, N; yellow, S and gray, C.

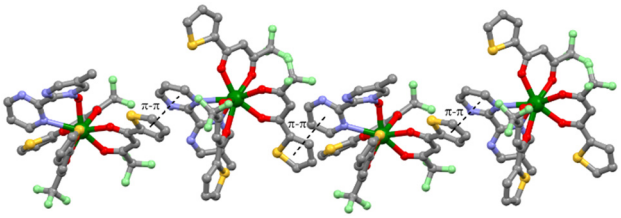

Fig. 8 Crystal packing of [Yb(tta)$_3$(L)] (**6**) highlighting the π–π stacking between the pyrazine and thiophene rings.

of the Yb(III) enantiomer is described hereafter with numerical values for Dy(III) in brackets. It crystallizes in the orthorhombic $P2_12_12_1$ space group (Table S1), and its asymmetric unit is composed of a binuclear complex (Fig. 9) of formula [Yb$_2$(hfc)$_6$(L)]. This complex could be seen as a chiral analogue of **1**. The ligand L bridges two Yb(III) ions through its two N–N and N–O coordination sites leading to an O7N biaugmented trigonal prism J50 coordination sphere around the Yb1 (CShM(C_{2v}) 0.966 [0.996]) (Table S2), while Yb2 adopted an O8 square antiprism environment (CShM(D_{4d}) 0.496 [0.534]) (Table S2).

The average Yb1–O, Yb2–O, Yb1–N and Yb2–N distances are 2.280(7) [2.324(12)] Å, 2.277(8) [2.319(11)] Å, 2.670(9) [2.702(14)] Å and 2.556(9) [2.595(14)] Å, respectively. The torsion angle defined by the angle made by the planes involving the two pyrazine rings was calculated to be 17.1(4) [17.4(5)]°. As already observed for **1**, the Yb(III) coordinated to the nitrogenated N–N chelating site imposes limited torsion between the pyrazine moieties. The shortest intramolecular and intermolecular Yb–Yb distances have been respectively measured to be 6.945(1) [7.020(2)] Å and 11.220(3) [11.206(2)] Å. Comparing the X-ray structures of **1** and **7**, one could conclude that replacing the hfac$^-$ anion with the bulkier hfc$^-$ one induced weak intramolecular modifications, *i.e.* a slight increase in both the torsion angle of L and the intramolecular Yb–Yb distance, but a drastic increase in the intermolecular Yb–Yb distance from 6.834(3) Å to 11.220(3) Å. The crystal packing revealed that the cohesion of the structure takes place through H···F and F···F short contacts. The phase purities of the four enantiomers were confirmed by powder X-ray diffraction investigation (Fig. S6 and S7).

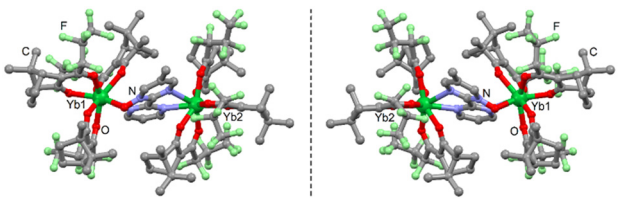

Fig. 9 Molecular structures of both enantiomers for [Yb$_2$(hfc)$_6$(L)], (–)**8** (left) and (+)**8** (right), determined from single crystal X-ray diffraction. Hydrogen atoms are omitted for clarity. Dark green, Yb; green, F; red, O; blue, N and gray, C.

Optical analysis: UV-visible absorption and natural circular dichroism measurements

[Ln$_2$(hfc)$_6$(L)] (Ln = Dy ((–)7, (+)7) and Yb ((–)8, (+)8)). The UV-visible absorption and natural circular dichroism (NCD) spectra for the complexes (–)**7**/(+)**7** and (–)**8**/(+)**8** have been measured in CH_2Cl_2 solution (Fig. 10). The experimental absorption curves for the two enantiomers of each complex are composed of broad bands localized in the 225–350 nm wavelength range. The absorption band at a high wavelength (250 nm) can be mainly attributed to the π–π* transitions of the L ligand, while those at lower energies are attributed to the (±)hfc$^-$ anions.[35]

The absolute values of the dissymmetry factor $|g_{abs}|$ have been calculated to be 6.8×10^{-4} at 295 nm and 1.2×10^{-3} at 340 nm (eqn (1)):

$$g_{abs} = \Delta\varepsilon/\varepsilon = (\varepsilon_L - \varepsilon_R)/(1/2(\varepsilon_L + \varepsilon_R)) \quad (1)$$

where $\Delta\varepsilon = \varepsilon_L - \varepsilon_R$ is the difference between the left (ε_L) and right (ε_R) molar absorption coefficients at the absorption wavelength.

Mirror images of the NCD spectra were observed, which confirm the enantiomeric nature of the complexes in CH_2Cl_2 solution at room temperature. A correspondence between the NCD and absorption bands can be observed. The NCD spectra mainly exhibit two negative (for (–)**7**/(–)**8**) and positive

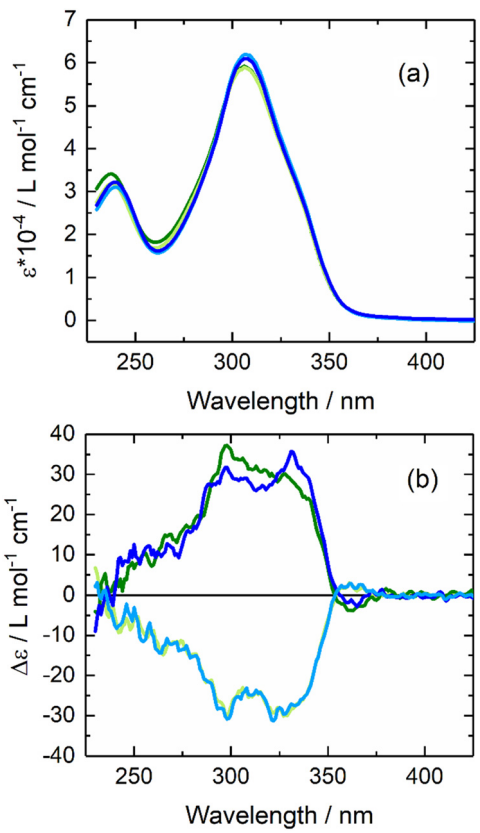

Fig. 10 Absorption (a) and natural circular dichroism (b) spectra of [(–)**7**] (light blue), [(+)**7**] (dark blue), [(–)**8**] (light green) and [(+)**8**] (dark green) in CH_2Cl_2 ($C = 1 \times 10^{-4}$ M).

(for (+)**7**/(+)**8**) contributions at 300 nm and 330 nm without an exciton CD couplet (Fig. 10), a sign of a lack of helical dispositions of the ligands around the lanthanide centre often associated with a square antiprismatic coordination geometry (SAPR). Even if one of the two lanthanide coordination environments has been determined in SAPR from the solid-state structural analysis, it is well-known that both solvent and concentration strongly affect the presence of the exciton CD couplet.[42,43]

Magnetic analysis

Static (dc) magnetic measurements. The room temperature values of the $\chi_M T$ product (where χ_M is the magnetic susceptibility) are 4.81 cm^3 K mol^{-1} for **1**, 27.28 cm^3 K mol^{-1} for **3**, 40.06 cm^3 K mol^{-1} for **4**, 2.33 cm^3 K mol^{-1} for **6**, 26.12 cm^3 K mol^{-1} for (+)**7** and 4.72 cm^3 K mol^{-1} for (+)**8** (Fig. S8–S13), which are in agreement with the expected values taking into account the 14.17 cm^3 K mol^{-1} and 2.57 cm^3 K mol^{-1} values for one isolated Dy(III) ion ($^6H_{15/2}$ ground state, g_J = 4/3) and one isolated Yb(III) ion ($^2F_{7/2}$ ground state, g_J = 8/7),[44] respectively. Upon decreasing the temperature, a continuous decrease of the $\chi_M T$ products for all the complexes was observed. At 2 K, the $\chi_M T$ products reach values of 2.13 cm^3 K mol^{-1} for **1**, 19.90 cm^3 K mol^{-1} for **3**, 28.81 cm^3 K mol^{-1} for **4**, 1.18 cm^3 K mol^{-1} for **6**, 19.52 cm^3 K mol^{-1} for (+)**7** and 2.65 cm^3 K mol^{-1} for (+)**8** (Fig. S8–S13). Such a decrease is mainly attributed to the depopulation of the M_J doublets when lowering the temperature. Significant intra- and intermolecular antiferromagnetic dipolar and exchange interactions between the Ln(III) ions at low temperature cannot be ruled out, especially in the case of the highly anisotropic Dy(III) ion.[28,34,36,44–47] The field dependences of the magnetization are depicted in Fig. S7–S12. At 50 kOe, $M(H)$ takes the values of 3.26 Nβ for **1**, 10.19 Nβ for **3**, 14.42 Nβ for **4**, 1.58 Nβ for **6**, 10.50 Nβ for (+)**7** and 3.24 Nβ for (+)**8**, which are far from the expected theoretical saturation values, a sign of significant magnetic anisotropy in all the molecular systems.

Dynamic (ac) magnetic measurements. First, the AC magnetic properties of the Yb(III) molecular systems (**1**, **6** and (+)**8**) were studied. The in-phase (χ'_M) and out-of-phase (χ''_M) components of the AC magnetic susceptibility were measured using immobilized microcrystalline samples. None of these complexes display slow magnetic relaxation under zero applied DC field, as observed in the literature.[48,49] Nevertheless, an out-of-phase signal of the magnetic susceptibility appears under an applied DC field (Fig. S14–S16). The field dependences of both χ'_M and χ''_M have been simultaneously fitted in the framework of the extended Debye model (eqn (S1), Tables S3–S5). The resulting τ *vs.* H curves at 2 K (Fig. S15 and S16) could be fitted using eqn (2):

$$\tau^{-1} = \frac{B_1}{1 + B_2 H^2} + 2B_3 H^m + B_4 \quad (2)$$

From left to right, the terms are the expressions of QTM, direct and thermally activated (Orbach + Raman) contributions. The best-fit parameters for m fixed to 4 are B_1 = 2.20(13) × 10^3 s^{-1}, B_2 = 4.52(4) × 10^{-5} Oe^{-2}, B_3 = 1.61(2) × 10^{-12} s^{-1} K^{-1} Oe^{-4} and B_4 = 9.48(2) × 10^2 s^{-1} for **6**, and B_1 = 3.15(3) × 10^4 s^{-1}, B_2 = 2.65(3) × 10^{-2} Oe^{-2}, B_3 = 1.00(2) × 10^{-12} s^{-1} K^{-1} Oe^{-4} and B_4 = 2.70(1) × 10^2 s^{-1} for (+)**8**. The fitting procedure highlights that QTM, thermally activated mechanisms, and direct magnetic relaxation processes are dominant in weak, moderate and high fields, respectively. The optimal DC field values have been selected to be 800 Oe for **1**, 1000 Oe for **6** and 1400 Oe for (+)**8**. Under such an applied field, the three Yb(III) complexes show frequency dependence of both χ'_M and χ''_M signals of the magnetization (Fig. S17–S19).

The two χ'_M and χ''_M signals have been simultaneously analysed in the framework of the extended Debye model (Tables S6–S8). The fraction of samples involved in the slow magnetic relaxation was determined from the normalized Argand plots to be equal to more than 90% for the three Yb(III) complexes (Fig. S20–S22). Notably, the remaining non-relaxing fraction is given by the interception of the semi-circle shape curve with the χ'_M/χ_T x-axis. Such observation implies that even if different coordination spheres around the Yb(III) ions have been identified for **1** and (+)**8**, they display similar magnetic behaviour under an applied dc field. Fig. 11 shows the thermal dependence of the relaxation time for the three complexes, which can be fitted using eqn (3):

$$\tau^{-1} = \underbrace{CT^n}_{\text{Raman}} + \underbrace{\tau_0^{-1} \exp\left(-\frac{\Delta}{kT}\right)}_{\text{Orbach}} \quad (3)$$

The best fits were obtained with a Raman process only with C = 1.25(19) × 10^3 K^{-n} s^{-1}, n = 3.41(15) for **1** and C = 8.0(5) K^{-n} s^{-1}, n = 5.02(5) for (+)**8** while a combination of Raman and Orbach processes was needed for **6** with C = 1.85(11) × 10^2

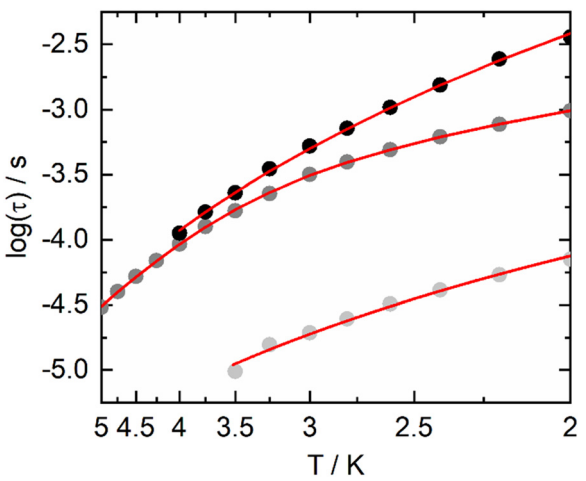

Fig. 11 Temperature dependence of the relaxation time under 800 Oe for **1** (full light grey circles), 1000 Oe for **6** (full grey circles) and 1400 Oe for (+)**8** (full black circles). The full red lines depict the best fits with parameters given in the text.

K^{-n} s^{-1}, n = 2.45(7) and τ_0 = 1.23(18) × 10^{-7} s^{-1} and Δ = 29.4(8) K, where C and n are the constant and exponential factors of the Raman process, and τ_0 and Δ are the relaxation time and energy barrier of the Orbach relaxation process, respectively. The expected n value for Kramers ions such as Yb(III) should be 9;[50] however, the presence of both acoustic and optical phonons in molecular systems can result in lower n values, typically between 2 and 7.[51–53] The relaxation time of the magnetization observed for the Yb(III)-based system slows down following the trend $hfac^-$ < tta^- < hfc^-, as already observed for other field-induced SMMs involving such Yb(β-diketonate)$_3$ units.[36] However, in addition to the hinderance effect of the β-diketonate, it cannot be ruled out that Yb(III) coordination geometry variation, as well as intra- and intermolecular Yb···Yb magnetic coupling play a role.

As already observed,[36] the complex involving the tta^- ancillary anion is the only one among the $hfac^-$, tta^-, $facam^-$ (3-(trifluoro-acetyl-(±)-camphorate)), hfc^- series which requires an Orbach contribution to reproduce the thermal dependence of the magnetic relaxation time.

In a second step, the dynamic studies of the magnetization were investigated for the two Dy(III) complexes **3** and **4**. Both complexes are composed of a similar binuclear unit, but **4** co-crystallizes with a Dy(hfac)$_3$(H$_2$O)$_2$ neutral complex, which strongly interacts with the binuclear unit through hydrogen bonds. For both complexes **3** and **4**, an out-of-phase signal was detected in zero applied magnetic field, but the maximum is localized at about 1 kHz for **3** (Fig. S23), while no maximum up to 10 kHz is observed for **4** at 2 K (Fig. S24). The application of an external DC field enabled the cancellation of the QTM[54] and a shift of the χ_M'' maxima to lower frequency is observed for **3** and **4**. Field dependence of the magnetic susceptibility for **3** and **4** was measured, and the relaxation times (τ) were extracted with an extended Debye model (eqn (S1) and Tables S9 and S10).[55–57] The resulting τ *vs.* H curves at 2 K (Fig. 12a and d) could be fitted using eqn (2). The best-fit parameters for m fixed to 4 are B_1 = 1.16(10) × 10^3 s^{-1}, B_2 = 1.61(16) × 10^{-5} Oe^{-2}, B_3 = 3.84(4) × 10^{-12} s^{-1} K^{-1} Oe^{-4} and B_4 = 22.8(4) s^{-1} for **3**, and B_1 = 2.29(9) × 10^5 s^{-1}, B_2 = 5.42(2) × 10^{-4} Oe^{-2}, B_3 = 1.12(2) × 10^{-11} s^{-1} K^{-1} Oe^{-4} and B_4 = 550(7) s^{-1} for **4**. At the optimal field and 2 K, the magnetic relaxation of **3** is 20 times slower than for **4**. Since the electronic distribution and symmetry (Table S2) for the Dy(III) coordination sphere composing the binuclear unit are identical for both complexes, the difference in the magnetic relaxation time might be attributed to an electronic effect and/or dipolar interaction between the binuclear and mononuclear units in **4**. Thus, the thermal dependence of the ac magnetic susceptibility was investigated at 0 Oe and 1600 Oe for **3** and only under 1200 Oe for **4**. Magnetic susceptibility has been analysed in the framework of the extended Debye model (Fig. 12b, c and e and S25–S27 and Tables S11–S13) and the resulting thermal dependences of the relaxation time have been fitted using eqn (4) for **3** and eqn (3) for **4** (Fig. 12f).

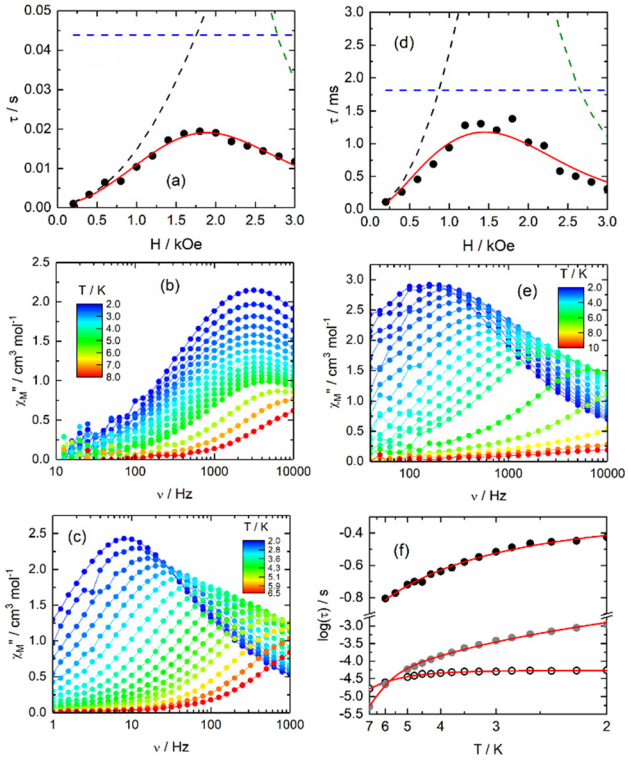

Fig. 12 Field dependence of the magnetic relaxation time (full black circles) at 2 K in the field range of 0–3000 Oe for **3** (a) and **4** (d) with the corresponding best fits depicted by the full red lines. The separated thermally activated Orbach + Raman, QTM and direct processes are shown by dashed blue, black and green lines, respectively. The frequency dependence of χ_M'' for **3** in the 2–8 K temperature range under a zero applied magnetic field (b) and in the 2–6.5 K temperature range under a 1600 Oe applied magnetic field (c). Frequency dependence of χ_M'' for **4** in the 2–10 K temperature range under a 1200 Oe applied magnetic field (e). (f) Thermal dependence of the magnetic relaxation time for **3** under zero applied magnetic field in the 2–7 K temperature range (open black circles), for **3** under a 1600 Oe applied magnetic field in the 2–6 K temperature range (full black circles) and for **4** under a 1200 Oe applied magnetic field in the 2–7 K temperature range (full grey circles). The full red lines are the best-fit curves (see text).

$$\tau^{-1} = \underbrace{CT^n}_{\text{Raman}} + \tau_{\text{QTM}}^{-1} \quad (4)$$

The best fits were obtained with a combination of QTM and Raman processes with τ_{QTM} = 5.30(4) × 10^{-5} s^{-1} and C = 8.22(2) K^{-n} s^{-1}, n = 4.39(1) for **3** at 0 Oe and τ_{QTM} = 0.57(4) s^{-1} and C = 0.27(9) K^{-n} s^{-1}, n = 1.59(2) for **3** at 1600 Oe, while a combination of Raman and Orbach processes was needed for **4** at 1200 Oe with C = 91.0(9) K^{-n} s^{-1}, n = 3.14(9) and τ_0 = 1.42(2) × 10^{-10} s^{-1} and Δ = 75.5(85) K. One could notice that a remaining QTM contribution was involved in the magnetic relaxation processes of **3** at 1600 Oe, as expected from the field dependence of the relaxation time (Fig. 12a). A stronger applied field would significantly activate the direct process. The fraction of samples involved in the slow magnetic relaxation was determined from the normalized Argand plots to be equal to more than 90% under an applied dc field for both complexes (Fig. S28–S30).

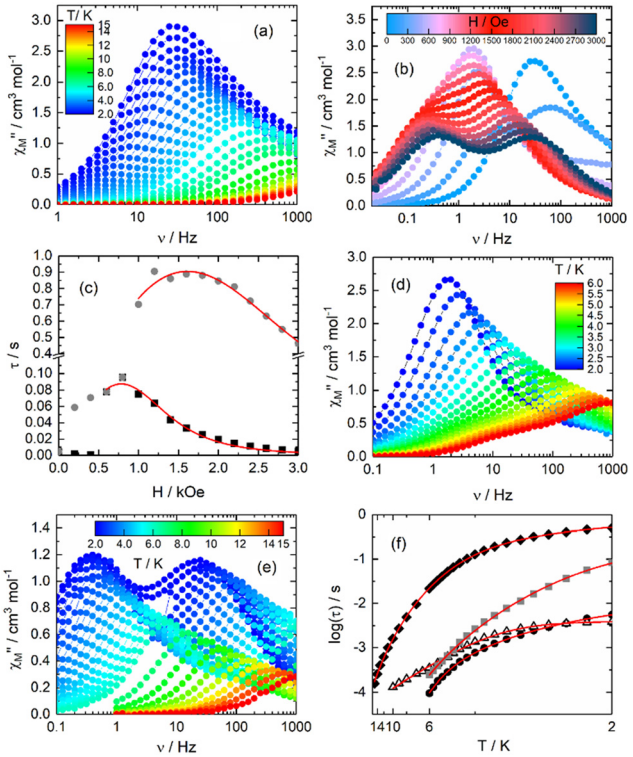

Fig. 13 (a) Frequency dependence of χ''_M for **(+)7** in the 2–15 K temperature range under a 0 Oe applied magnetic field. (b) Field dependence of χ''_M in the 0–3000 Oe field range at 2 K. (c) Field dependence of the magnetic relaxation time at 2 K in the field range of 0–3000 Oe for the HF contribution (τ_1, full black squares) and the LF contribution (τ_2, full grey circles) with the corresponding best fits shown as full red lines. (d) Frequency dependence of χ''_M for **(+)7** in the 2–6 K temperature range under a 600 Oe applied magnetic field. (e) Frequency dependence of χ''_M for **(+)7** in the 2–15 K temperature range under a 3000 Oe applied magnetic field. (f) Thermal dependence of the magnetic relaxation time for **(+)7** under zero applied magnetic field in the 2–10 K temperature range (open black triangles), under a 600 Oe applied magnetic field in the 2–6 K temperature range (full grey squares) and under a 3000 Oe applied magnetic field in the 2–15 K temperature range (τ_1, full black squares) and 2–6 K temperature range (τ_2, full black circles). Full red lines are the best-fit curves (see text).

Finally, the AC magnetic properties of **(+)7** were investigated. The field dependence of the magnetic susceptibility measured at 2 K demonstrated a slow magnetic relaxation at zero applied DC field (Fig. 13b and S31). In the absence of a DC field, the thermal dependence of the magnetic susceptibility was analysed in the framework of the extended Debye model (Fig. 13a and S32 and Table S14). The resulting thermal dependence of the relaxation time has been fitted using eqn (5) (Fig. 13f):

$$\tau^{-1} = \tau_{QTM}^{-1} + \underbrace{\tau_0^{-1}\exp\left(-\frac{\Delta}{kT}\right)}_{\text{Orbach}} \quad (5)$$

The best fits were obtained with a combination of Orbach and QTM with $\tau_0 = 2.06(11) \times 10^{-5}$ s^{-1}, $\Delta = 18.2(3)$ K and $\tau_{QTM} = 3.92(10) \times 10^{-3}$ s^{-1}. The normalized Argand plot displays a semicircular curve in agreement with a fraction of more than 85% of the sample involved in the slow magnetic relaxation (Fig. S33). Thus, at 0 Oe, the two Dy(III) centers relax at the same rate despite the two different coordination environments. To cancel the fast magnetic relaxation through the QTM process, an external DC field was applied.

For weak applied DC (<750 Oe), an almost single χ''_M contribution shifting to lower frequency was observed. However, for a stronger applied DC field, the χ''_M contribution splits into two signals. The relaxation times (τ) were extracted from the field dependence of the magnetic susceptibility with an extended Debye model, accounting for two relaxation contributions (eqn (S2) and Table S15).[25–27] The resulting τ *vs.* H curves at 2 K (Fig. 13c and S34) could be fitted using eqn (2). The best-fit parameters for m fixed to 4 are $B_1 = 6.87(6) \times 10^3$ s^{-1}, $B_2 = 4.52(4) \times 10^{-3}$ Oe^{-2}, $B_3 = 1.64(3) \times 10^{-12}$ s^{-1} K^{-1} Oe^{-4} and $B_4 = 7.69(4)$ s^{-1} for the high-frequency (HF) contribution and $B_1 = 6.17(2) \times 10^3$ s^{-1}, $B_2 = 1.12(4) \times 10^{-2}$ Oe^{-2}, $B_3 = 7.78(8) \times 10^{-15}$ s^{-1} K^{-1} Oe^{-4} and $B_4 = 0.79(23)$ s^{-1} for the low-frequency (LF) contribution. Then, the dynamic magnetic properties of **(+)7** were investigated under weak (600 Oe) and strong (3000 Oe) applied dc fields. Under 600 Oe, the thermal dependence of the magnetic susceptibility (Fig. 13d and S35) was analysed in the framework of the extended Debye model (eqn (S1) and Table S16), accounting for a single relaxation distribution because $\tau_1 \cong \tau_2$ (Fig. S34). The resulting thermal dependences of the relaxation time have been fitted using eqn (4) (Fig. 13f). The best fit was obtained with a combination of QTM and Raman processes with $\tau_{QTM} = 0.23(4)$ s^{-1} and $C = 0.15(2)$ K^{-n} s^{-1}, $n = 5.69(7)$. The normalized Argand plot for **(+)7** at 600 Oe confirmed that the two Dy(III) ions are involved in the slow magnetic relaxation with a single rate for $T < 5$ K (Fig. S36). Under 3000 Oe, the thermal dependence of the magnetic susceptibility (Fig. 13e and S37) highlights two contributions associated with the two Dy(III) ions in different environments. Thus, both χ'_M and χ''_M were analysed in the framework of the extended Debye model (eqn (S2) and Table S17) accounting for two relaxation distributions. The resulting thermal dependences of the relaxation time have been fitted using eqn (6) (Fig. 13f). The best fit was obtained with a combination of Raman, Orbach and direct processes for τ_1 (HF) with $C = 4.78(17)$ K^{-n} s^{-1}, $n = 3.89(25)$; $\tau_0 = 1.33(12) \times 10^{-8}$ s^{-1}, $\Delta = 57.9(60)$ K and $A = 6.80(9) \times 10^{-13}$ Oe^{-m} K^{-1} s^{-1} with $m = 4$ (fixed) and a combination of Raman and direct processes for τ_2 (LF) with $C = 2.37(14) \times 10^{-3}$ K^{-n} s^{-1}, $n = 5.43(3)$ and $A = 1.12(2) \times 10^{-14}$ Oe^{-m} K^{-1} s^{-1} with $m = 4$ (fixed).

$$\tau^{-1} = \underbrace{CT^n}_{\text{Raman}} + \underbrace{AH^4T}_{\text{Direct}} \quad (6)$$

$$\tau^{-1} = \underbrace{CT^n}_{\text{Raman}} + \underbrace{\tau_0^{-1}\exp\left(-\frac{\Delta}{kT}\right)}_{\text{Orbach}} + \underbrace{AH^4T}_{\text{Direct}} \quad (7)$$

Based on the previously published i) binuclear Dy(III) complexes with L and other β-diketonates (tta$^-$ and tmh$^-$ =

2,2,6,6-tetramethyl-3,5-heptanedionate)[37] and ii) SMMs involving Dy(β-diketonate)$_3$ in which the Dy(III) center adopted a N2O6 coordination sphere,[58,59] the τ_1 and τ_2 are respectively associated with the Dy(III) in NO7 and N2O6 environments. The normalized Argand plot for **(+)7** at 3000 Oe is shown in Fig. S38, showing two semicircles of similar intensity at a given temperature, and each of them represents 50% of the slow magnetic relaxation fraction.

Conclusions

A series of coordination reactions between 4-methyl-2,2′-bipyrimidine-2-oxide and several Ln(β-diketonate)$_3$(H$_2$O)$_n$ metal building blocks (Ln(III) = Dy and Yb with n = 1 or 2; hfac$^-$ = 1,1,1,5,5,5-hexafluoroacetylacetonate, tta$^-$ = 2-thenoytrifluoroacetylacetonate, and hfc$^-$ = [3-(heptafluoropropylhydroxymethylene)-D/L-camphorate] anion) has been performed. Ten lanthanide complexes have been designed, one mononuclear complex [Yb(tta)$_3$(L)] (**6**), two dinuclear complexes [Yb$_2$(hfac)$_6$(L)] (**1**) and [Dy(hfac)$_3$(L)]$_2$·C$_2$H$_4$Cl$_2$ (**3**)·C$_2$H$_4$Cl$_2$, four dinuclear enantiomers [Ln$_2$(hfc)$_6$(L)] (Ln = Dy **(−)7**, **(+)7** and Yb **(−)8**, **(+)8**), one trinuclear complex [Dy(hfac)$_3$(L)]$_2$[Dy(hfac)$_3$(H$_2$O)$_2$] (**4**) and two hexanuclear complexes [Ln$_6$(hfac)$_{14}$(OH)$_4$(L)$_2$] (Ln = Yb (**2**) and Dy (**5**)). The final molecular architecture of the systems depends on the ratio between the metallo-precursor and L and on the nature/bulkiness of the β-diketonate anion. All the Yb(III)-based systems displayed field-induced slow magnetic relaxation with magnetic relaxation occurring mainly through a Raman process with the relaxation time adopting the following trend: hfac$^-$ < tta$^-$ < hfc$^-$. The two Dy(III) dinuclear complexes **3** and **(±)7** display such magnetic behaviour at zero applied DC field, whereas the co-crystallization with Dy(hfac)$_3$(H$_2$O)$_2$ (complex **4**) induced only field-activated-SMM behaviour, demonstrating that the presence of a close Dy(III) ion interacting through hydrogen bonds has a significant influence on the dynamic magnetic properties of the dinuclear unit. **(+)7** displayed zero-field SMM behaviour despite the two Dy(III) centers being in different coordination spheres. The application of an external DC field induced the expected multi-SMM phenomenon. However, the Yb(III) analogue did not exhibit such a multi-contribution of its slow magnetic relaxation in an applied DC field.

The systematic additional Orbach contribution to the Raman process in the slow magnetic relaxation of Yb(III) complexes involving tta$^-$ anions, as well as the absence of a multi-relaxation phenomenon for Yb(III) field-induced SMMs, are under investigation in our group.

Experimental

Synthesis: general procedures and materials

The precursors Ln(β-diketonate)$_3$(H$_2$O)$_n$ (Ln(III) = Dy and Yb with n = 1 or 2; hfac$^-$ = 1,1,1,5,5,5-hexafluoroacetylacetonate,[60] tta$^-$ = 2-thenoytrifluoroacetylacetonate,[61] hfc$^-$ = [3-(heptafluoropropylhydroxymethylene)-D/L-camphorate][62] anion), and the ligand 4-methyl-2,2′-bipyrimidine-2-*N*-oxide (**L**)[37] were synthesized following previously reported methods. All other chemicals used were of analytical reagent grade quality.

Synthesis of [Yb$_2$(hfac)$_6$(L)] (1). 83.0 mg of Yb(hfac)$_3$(H$_2$O)$_2$ (0.1 mmol) were dissolved in 10 mL of CH$_2$Cl$_2$ and then added to a solution of 10 mL of CH$_2$Cl$_2$ containing 9.4 mg of **L** (0.05 mmol). After 30 min of stirring, 30 mL of *n*-hexane were layered at room temperature in the dark. Slow diffusion leads to colorless prismatic single crystals of **1** which are suitable for X-ray diffraction studies. Yield 67.5 mg (76%). Anal. calcd (%) for C$_{39}$H$_{14}$F$_{36}$N$_4$O$_{13}$Yb$_2$: C 26.35, H 0.79, N 3.15; found: C 26.49, H 0.81 N, 3.11. Representative I.R. bands (KBr): 3303, 3149, 3102, 1654, 1615, 1562, 1540, 1417, 1247, 1141, 1103, 804, 740, 669 and 590 cm^{-1}. Additional colorless plates suitable for single crystal X-ray diffraction have been identified as a hexanuclear complex of formula [Yb$_6$(hfac)$_{14}$(OH)$_4$(**L**)$_2$] (**2**) in a very minor phase.

Synthesis of [Dy(hfac)$_3$(L)]$_2$·C$_2$H$_4$Cl$_2$ ((3)·C$_2$H$_4$Cl$_2$). 41.5 mg of Dy(hfac)$_3$(H$_2$O)$_2$ (0.05 mmol) were dissolved in 5 mL of dichloroethane (C$_2$H$_4$Cl$_2$) and then added to a solution of 10 mL of C$_2$H$_4$Cl$_2$ containing 9.4 mg of **L** (0.05 mmol). After 45 min of stirring and heating at 80 °C, slow diffusion of *n*-hexane leads to colorless single crystals, which are suitable for X-ray diffraction studies. Yield 31.6 mg (65%). Anal. calcd (%) for C$_{48}$H$_{22}$Dy$_2$F$_{36}$N$_8$O$_{14}$ (**3**): C 29.64, H 1.16, N 5.76; found: C 29.59, H 1.09, N 5.84. Representative I.R. bands (KBr): 3144, 3058, 1659, 1557, 1533, 1508, 1416, 1378, 1262, 1210, 1151, 1102, 1011, 947, 885, 802, 745, 661, 584, 522 and 468 cm^{-1}.

Synthesis of [Dy(hfac)$_3$(L)]$_2$[Dy(hfac)$_3$(H$_2$O)$_2$] (4). 62.3 mg of Dy(hfac)$_3$(H$_2$O)$_2$ (0.075 mmol) were dissolved in 10 mL of CH$_2$Cl$_2$ and then added to a solution of 10 mL of CH$_2$Cl$_2$ containing 9.4 mg of **L** (0.05 mmol). After 30 min of stirring, 30 mL of *n*-hexane were layered at room temperature in the dark. Slow diffusion leads to colorless single crystals which are suitable for X-ray studies. Yield 42.1 mg (61%). Anal. calcd (%) for C$_{63}$H$_{29}$Dy$_3$F$_{54}$N$_8$O$_{22}$: C 27.37, H 1.05, N 4.05; found: C 27.39, H 1.06 N, 4.11. Representative I.R. bands (KBr): 3657, 3420, 1659, 1644, 1562, 1538, 1495, 1416, 1257, 1209, 1146, 1097, 802, 1146, 793, 734, 657 and 579 cm^{-1}. An additional pale yellow material suitable for single crystal X-ray diffraction has been identified as a hexanuclear complex of formula [Dy$_6$(hfac)$_{14}$(OH)$_4$(**L**)$_2$] (**5**) in a very minor phase.

Synthesis of [Yb(tta)$_3$(L)] (6). 43.6 mg of Yb(tta)$_3$(H$_2$O)$_2$ (0.05 mmol) were dissolved in 5 mL of dry toluene and then added to a solution of 10 mL of dry toluene containing 9.4 mg of **L** (0.05 mmol). After stirring for 1 h at 80 °C, slow diffusion of *n*-hexane leads to pale yellow single crystals, which are suitable for X-ray diffraction studies. Yield 39.9 mg (78%). Anal. calcd (%) for C$_{33}$H$_{20}$F$_9$N$_4$O$_7$S$_3$Yb: C 38.67, H 1.95, N 5.47; found: C 38.49, H 2.01 N, 5.44. Representative I.R. bands (KBr): 3435, 3111, 1600, 1542, 1509, 1470, 1446, 1412, 1354, 1306, 1247, 1223, 1179, 1205, 1136, 1054, 928, 793, 725, 638 and 579 cm^{-1}.

Synthesis of $[Ln_2(hfc)_6(L)]$ (Ln = Dy ((−)7, (+)7) and Yb ((−)8, (+)8)). 0.1 mmol of $Ln(hfc)_3(H_2O)$ (Ln = Dy 122.2 mg, Yb 123 mg) were dissolved in 15 mL of *n*-heptane and then added to a solution of 15 mL of $CHCl_3$ containing 9.4 mg of **L** (0.05 mmol). After 30 min of stirring at room temperature, slow evaporation leads to yellow single crystals which are suitable for X-ray diffraction studies. Yields 79.1 mg (61%) for (−)7, 85.6 mg (66%) for (+)7, 77.2 mg (59%) for (−)8, 90.3 mg (69%) for (+)8. Anal. calcd (%) for $C_{93}H_{92}Dy_2F_{42}N_4O_{13}$ ((−)7): C 43.01, H 3.55, N 2.16; found: C 43.09, H 3.56 N, 2.24. Anal. calcd (%) for $C_{93}H_{92}Dy_2F_{42}N_4O_{13}$ ((+)7): C 43.01, H 3.55, N 2.16; found: C 43.05, H 3.61, N 2.21. Anal. calcd (%) for $C_{93}H_{92}Yb_2F_{42}N_4O_{13}$ ((−)8): C 42.66, H 3.52, N 2.14; found: C 42.71, H 3.46, N 2.09. Anal. calcd (%) for $C_{93}H_{92}Yb_2F_{42}N_4O_{13}$ ((+)8): C 42.66, H 3.52, N 2.14; found: C 42.69, H 3.51, N 2.17. Representative I.R. bands (KBr): 3367, 3052, 1595, 1553, 1518, 1465, 1407, 1306, 1218, 1059, 1465, 1020, 753, 720, 686, 604 and 507 cm^{-1}.

Crystallography

Single crystals of **1**–**6**, (−)7, (−)8 and (+)8 were mounted on an APEXII Bruker-AXS diffractometer for data collection (MoK_α radiation source, λ = 0.71073 Å), from the Centre de Diffractométrie X (CDIFX), Université de Rennes, France, while a single crystal of (+)7 was mounted on a D8 VENTURE Bruker-AXS diffractometer (Table S1).

Structures were solved by the direct method using the SHELXT program[63] and refined by full matrix least-squares method on F^2 using the SHELXL-14/7 program.[64] The SQUEEZE procedure of PLATON[65] was performed as the structures for **1**, **2**, **5**, **6**, (−)7, (+)7, (−)8 and (+)8 contain large solvent accessible voids for which residual peaks of diffraction were observed. Complete crystal structure results as a CIF file are deposited as SI. CCDC numbers are 2482203–2482212 for complexes **1**, **2**, **5**, **6**, (−)7, (+)7, (−)8 and (+)8. Powder X-ray diffraction (PXRD) patterns for all samples were recorded at room temperature in the 2θ range of 5–30° with a step size of 0.026° and a scan time per step of 600 s using a PANalytical X'Pert Pro diffractometer (Cu-L2,L3 radiation, λ = 1.5418 Å, 40 kV, 40 mA, PIXcel 1D detector). Data collector and HighScore Plus software were used, respectively, for recording and analysing the patterns.

Physical measurements

The elemental analyses of the complexes were performed at the Centre Régional de Mesures Physiques de l'Ouest, Rennes. Absorption spectra were recorded on a JASCO V-650 spectrophotometer in dilute solution by using spectrophotometric-grade solvents. Electronic circular dichroism (ECD) was measured on a JASCO J-815 Circular Dichroism Spectrometer (IFR140 facility-Biosit_Université de Rennes). A Quantum Design MPMS-XL SQUID magnetometer was used to measure the DC magnetic susceptibility for solid polycrystalline samples. 0.2 kOe, 2 kOe and 10 kOe magnetic fields are applied, respectively, for the temperature ranges of 2–20 K, 20–80 K and 80–300 K. In AC mode, an oscillating field of 3 Oe is applied at frequencies between 1 and 1000 Hz with a Quantum Design MPMS-XL and an oscillating field of 5 Oe is applied at frequencies between 10 and 10 000 Hz with a Quantum Design PPMS. For all samples, the magnetization is corrected for intrinsic diamagnetism evaluated using Pascal's tables and the extrinsic diamagnetism of the sample holder (Teflon tape). These measurements were all corrected for the diamagnetic contribution as calculated using Pascal's constants. The AC magnetic susceptibility measurements were performed on the same apparatus.

Author contributions

H. D. and B. L. performed the organic synthesis, coordination chemistry, crystallizations and PXRD. V. D. realised the single crystal X-ray diffraction experiments and refined the X-ray structures. J. F. G. carried out the magnetic measurements. F. P. conceived and designed the experiments, interpreted the magnetic measurements and drove the writing of the article. All authors have read and agreed on the published version of the manuscript.

Conflicts of interest

The authors declare no conflicts of interest.

Data availability

The data that support the findings of this study are available in the supplementary information (SI) of this article. The authors will supply the relevant data in response to reasonable requests.

Supplementary information: SCXRD parameters, CSM calculated results, PXRD patterns and additional magnetic data. See DOI: https://doi.org/10.1039/d5ce00831j.

CCDC 2482203–2482212 contain the supplementary crystallographic data for this paper.[66a–j]

Acknowledgements

This work was supported by CNRS, Université de Rennes and the European Research Council through the ERC-CoG 725184 MULTIPROSMM (project no. 725184). Part of this work has been performed using the Spectroscopies-DCTP core facility (UMS Biosit, Université de Rennes – Campus de Villejean – 35043 RENNES Cedex, FRANCE).

Notes and references

1 N. Ishikawa, M. Sugita, T. Ishikawa, S. Koshihara and Y. Kaizu, *J. Am. Chem. Soc.*, 2003, **125**, 8694–8695.
2 J. D. Rinehart and J. R. Long, *Chem. Sci.*, 2011, **2**, 2078–2085.
3 C. A. P. Goodwin, F. Ortu, D. Reta, N. F. Chilton and D. Mills, *Nature*, 2017, **548**, 439–442.

4 F.-S. Guo, B. M. Day, Y.-C. Chen, M.-L. Tong, A. Mansikkamäki and R. A. Layfield, *Angew. Chem., Int. Ed.*, 2017, **56**, 11445–11449.
5 F.-S. Guo, B. M. Day, Y.-C. Chen, M.-L. Tong, A. Mansikkamäki and R. A. Layfield; Corrigendum:F.-S. Guo, B. M. Day, Y.-C. Chen, M.-L. Tong, A. Mansikkamäki and R. A. Layfield, *Angew. Chem., Int. Ed.*, 2020, **59**, 18844.
6 K. R. McClain, C. A. Gould, K. Chakarawet, S. J. Teat, T. J. Groshens, J. R. Long and B. G. Harvey, *Chem. Sci.*, 2018, **9**, 8492–8503.
7 F.-S. Guo, B. M. Day, Y.-C. Chen, M.-L. Tong, A. Mansikkamäki and R. A. Layfield, *Science*, 2018, **362**, 1400–1403.
8 P. E. Evans, D. Reta, G. F. S. Whitehead, N. F. Chilton and D. P. Mills, *J. Am. Chem. Soc.*, 2019, **141**, 19935–19940.
9 C. A. Gould, K. R. McClain, D. Reta, J. G. C. Kragskow, D. A. Marchiori, E. Lachman, E.-S. Choi, J. G. Analytis, R. D. Britt, N. F. Chilton, B. G. Harvey and J. R. Long, *Science*, 2022, **375**, 198–202.
10 F.-S. Guo, M. He, G.-Z. Huang, S. R. Giblin, D. Billington, F. W. Heinemann, M.-L. Tong, A. Mansikkamäki and R. A. Layfield, *Inorg. Chem.*, 2022, **61**, 6017–6025.
11 J. C. Vanjak, B. O. Wilkins, V. Vieru, N. S. Bhuvanesh, J. H. Reibenspies, C. D. Martin, L. F. Chibotaru and M. Nippe, *J. Am. Chem. Soc.*, 2022, **144**, 17743–17747.
12 A. H. Vincent, Y. L. Whyatt, N. F. Chilton and J. R. Long, *J. Am. Chem. Soc.*, 2023, **145**, 1572–1579.
13 G. K. Gransbury, S. C. Corner, J. G. C. Kragskow, P. Evans, H. M. Yeung, W. J. A. Blackmore, G. F. S. Whitehead, I. J. Vitorica-Yrezabal, M. S. Oakley, N. F. Chilton and D. P. Mills, *J. Am. Chem. Soc.*, 2023, **145**, 22814–22825.
14 J. Emerson-King, G. K. Gransbury, B. E. Atkinson, W. J. A. Blackmore, G. F. S. Whitehead, N. F. Chilton and D. P. Mills, *Nature*, 2025, **643**, 125–129.
15 J. D. Rinehart, M. Fang, W. J. Evans and J. R. Long, *Nat. Chem.*, 2011, **3**, 538–542.
16 S. Demir, J. M. Zadrozny, M. Nippe and J. R. Long, *J. Am. Chem. Soc.*, 2012, **134**, 18546–18549.
17 M. Mannini, F. Pineider, P. Sainctavit, C. Danieli, E. Otero, C. Sciancalepore, A. M. Talarico, M.-A. Arrio, A. Cornia, D. Gatteschi and R. Sessoli, *Nat. Mater.*, 2009, **8**, 194–197.
18 S. Thiele, F. Balestro, R. Ballou, S. Klyatskaya, M. Ruben and W. Wernsdorfer, *Science*, 2014, **344**, 1135–1138.
19 K. S. Pedersen, A.-M. Ariciu, S. McAdams, H. Weihe, J. Bendix, F. Tuna and S. Piligkos, *J. Am. Chem. Soc.*, 2016, **138**, 5801–5804.
20 X. Yi, G. Calvez, C. Daiguebonne, O. Guillou and K. Bernot, *Inorg. Chem.*, 2015, **54**, 5213–5219.
21 T. Han, W. Shi, X. P. Zhang, L. L. Li and P. A. Cheng, *Inorg. Chem.*, 2012, **51**, 13009–13016.
22 S. V. Eliseeva, M. Ryazanov, F. Gumy, S. I. Troyanov, L. S. Lepnev, J. C. G. Bünzli and N. P. Kuzmina, *Eur. J. Inorg. Chem.*, 2006, 4809–4820.
23 K. Murashima, S. Karasawa, K. Yoza, Y. Inagaki and N. Koga, *Dalton Trans.*, 2016, **45**, 7067–7077.
24 E. Kiefl, M. Mannini, K. Bernot, X. Yi, A. Amato, T. Leviant, A. Magnani, T. Prokscha, A. Suter, R. Sessoli and Z. Salman, *ACS Nano*, 2016, **10**, 5663–5669.
25 W. Zhu, X. Xiong, C. Gao, S. Li, Y. Zhang, J. Wang, C. Zhang, A. Powell and S. Gao, *Dalton Trans.*, 2017, **46**, 14114–14121.
26 F. Pointillart, Y. Le Gal, S. Golhen, O. Cador and L. Ouahab, *Inorg. Chem.*, 2009, **48**, 4631–4633.
27 F. Pointillart, T. Cauchy, O. Maury, Y. Le Gal, S. Golhen, O. Cador and L. Ouahab, *Chem. – Eur. J.*, 2010, **16**, 11926–11941.
28 F. Pointillart, Y. Le Gal, S. Golhen, O. Cador and L. Ouahab, *Chem. – Eur. J.*, 2011, **17**, 10397–10404.
29 F. Pointillart, B. Le Guennic, S. Golhen, O. Cador, O. Maury and L. Ouahab, *Chem. Commun.*, 2013, **49**, 615–617.
30 F. Pointillart, B. Le Guennic, T. Cauchy, S. Golhen, O. Cador, O. Maury and L. Ouahab, *Inorg. Chem.*, 2013, **52**, 5978–5990.
31 F. Pointillart, B. Le Guennic, S. Golhen, O. Cador and L. Ouahab, *Chem. Commun.*, 2013, **49**, 11632–11634.
32 F. Pointillart, B. Le Guennic, S. Golhen, O. Cador, O. Maury and L. Ouahab, *Inorg. Chem.*, 2013, **52**, 1610–1620.
33 M. Feng, F. Pointillart, B. Lefeuvre, V. Dorcet, S. Golhen, O. Cador and L. Ouahab, *Inorg. Chem.*, 2015, **54**, 4021–4028.
34 F. Pointillart, T. Guizouarn, B. Lefeuvre, S. Golhen, O. Cador and L. Ouahab, *Chem. – Eur. J.*, 2015, **21**, 16929–16934.
35 H. Douib, J. Flores Gonzalez, S. Speed, V. Montigaud, B. Lefeuvre, V. Dorcet, F. Riobé, O. Maury, A. Gouasmia, B. Le Guennic, O. Cador and F. Pointillart, *Dalton Trans.*, 2022, **51**, 16486–16496.
36 H. Douib, B. Lefeuvre, K. Dhbaibi, J. Flores Gonzalez, V. Dorcet and F. Pointillart, *Chem. – Asian J.*, 2025, e202500234.
37 I. F. Diaz-Ortega, J. Manuel Herrera, D. Aravena, E. Ruiz, T. Gupta, G. Rajaraman, H. Nojiri and E. Colacio, *Inorg. Chem.*, 2018, **57**, 6362–6375.
38 J. Long, M. S. Ivanov, V. A. Khomchenko, E. Mamontova, J.-M. Thibaud, J. Rouquette, M. Beaudhuin, D. Granier, R. A. S. Ferreira, L. D. Carlos, B. Donnadieu, M. S. C. Henriques, J. A. Paixao, Y. Guari and J. Larionova, *Science*, 2020, **367**, 671–676.
39 K. Wang, S. Zeng, H. Wang, J. Dou and J. Jiang, *Inorg. Chem. Front.*, 2014, **1**, 167–171.
40 M. Atzori, K. Dhbaibi, H. Douib, M. Grasser, V. Dorcet, I. Breslavetz, K. Paillot, O. Cador, G. L. J. A. Rikken, B. Le Guennic, J. Crassous, F. Pointillart and C. Train, *J. Am. Chem. Soc.*, 2021, **143**, 2671–2675.
41 M. Llunell, D. Casanova, J. Cirera, P. Alemany and S. Alvarez, *SHAPE Program for the Stereochemical Analysis of Molecular Fragments by Means of Continuous Shape Measures and Associated Tools*, Departament de Quimica Fisica, Departament de Quimica Inorganica, and Institut de Quimica Teorica i Computacional – Universitat dè Barcelona, Barcelona, Spain, 2013.
42 D. Shirotani, T. Susuki, K. Yamanari and S. Kaizaki, *J. Alloys Compd.*, 2008, **451**, 325–328.
43 J. L. Lunkley, D. Shirotani, K. Yamanari, S. Kaizaki and G. Muller, *J. Am. Chem. Soc.*, 2008, **130**, 13814–13815.

44 J. Long, F. Habib, P.-H. Lin, I. Korobkov, G. Enright, L. Ungur, W. Wernsdorfer, L. F. Chibotaru and M. Murugesu, *J. Am. Chem. Soc.*, 2011, **133**, 5319–5328.
45 Y. N. Guo, G. F. Xu, W. Wernsdorfer, L. Ungur, Y. Guo, J. Tang, H.-J. Zhang, L. F. Chibotaru and A. K. Powell, *J. Am. Chem. Soc.*, 2011, **133**, 11948–11951.
46 F. Pointillart, B. Le Guennic, O. Maury, S. Golhen, O. Cador and L. Ouahab, *Inorg. Chem.*, 2013, **52**, 1398–1408.
47 C. Y. Chow, H. Bolvin, V. E. Campbell, R. Guillot, J. W. Kampf, W. Wernsdorfer, F. Gendron, J. Autschbach, V. L. Pecoraro and T. Mallah, *Chem. Sci.*, 2015, **6**, 4148–4159.
48 F. Pointillart, O. Cador, B. Le Guennic and L. Ouahab, *Coord. Chem. Rev.*, 2017, **346**, 150–175.
49 A. Borah and R. Murugavel, *Coord. Chem. Rev.*, 2022, **453**, 214288.
50 C. Dekker, A. F. M. Arts, H. W. de Wijn, A. J. van Duyneveldt and J. A. Mydosh, *Phys. Rev. B: Condens. Matter Mater. Phys.*, 1989, **40**, 11243–11251.
51 J. Tang and P. Zhang, *Lanthanide Single Molecule Magnets*, Springer, Berlin, Germany, 2015.
52 P. Evans, D. Reta, G. F. S. Whitehead, N. F. Chilton and D. P. Mills, *J. Am. Chem. Soc.*, 2019, **141**, 19935–19940.
53 D. Reta and N. F. Chilton, *Phys. Chem. Chem. Phys.*, 2019, **21**, 23567–23575.
54 L. Thomas, F. Lionti, R. Ballou, D. Gatteschi, R. Sessoli and B. Barbara, *Nature*, 1996, **383**, 145–147.
55 K. S. Cole and R. H. Cole, *J. Chem. Phys.*, 1941, **9**, 341–351.
56 R. Orbach, *Proc. R. Soc. London, Ser. A*, 1961, **264**, 458–484.
57 R. Orbach, *Proc. Phys. Soc., London*, 1961, **77**, 821–826.
58 F. Pointillart, J. Jung, R. Berraud-Pache, B. Le Guennic, V. Dorcet, S. Golhen, O. Cador, O. Maury, Y. Guyot, S. Decurtins, S.-X. Liu and L. Ouahab, *Inorg. Chem.*, 2015, **54**, 5384–5397.
59 T. T. Da Cunha, J. Jung, M.-E. Boulon, G. Campo, F. Pointillart, C. L. M. Pereira, B. Le Guennic, O. Cador, K. Bernot, F. Pineider, S. Golhen and L. Ouahab, *J. Am. Chem. Soc.*, 2013, **135**, 16332–16335.
60 M. F. Richardson, W. F. Wagner and D. E. Sands, *J. Inorg. Nucl. Chem.*, 1968, **30**, 1275–1289.
61 A. I. Vooshin, N. M. Shavaleev and V. P. Kazakov, *J. Lumin.*, 2000, **91**, 49–58.
62 I. Ghosh, H. Zeng and Y. Kishi, *Org. Lett.*, 2004, **6**, 4715–4718.
63 G. M. Sheldrick, *Acta Crystallogr., Sect. A: Found. Adv.*, 2015, **71**, 3–8.
64 G. M. Sheldrick, *Acta Crystallogr., Sect. C: Struct. Chem.*, 2015, **71**, 3–8.
65 A. L. Spek, *J. Appl. Crystallogr.*, 2003, **36**, 7–13.
66 (*a*) CCDC 2482203: Experimental Crystal Structure Determination, 2025, DOI: 10.5517/ccdc.csd.cc2p9y21; (*b*) CCDC 2482204: Experimental Crystal Structure Determination, 2025, DOI: 10.5517/ccdc.csd.cc2p9y32; (*c*) CCDC 2482205: Experimental Crystal Structure Determination, 2025, DOI: 10.5517/ccdc.csd.cc2p9y43; (*d*) CCDC 2482206: Experimental Crystal Structure Determination, 2025, DOI: 10.5517/ccdc.csd.cc2p9y54; (*e*) CCDC 2482207: Experimental Crystal Structure Determination, 2025, DOI: 10.5517/ccdc.csd.cc2p9y65; (*f*) CCDC 2482208: Experimental Crystal Structure Determination, 2025, DOI: 10.5517/ccdc.csd.cc2p9y76; (*g*) CCDC 2482209: Experimental Crystal Structure Determination, 2025, DOI: 10.5517/ccdc.csd.cc2p9y87; (*h*) CCDC 2482210: Experimental Crystal Structure Determination, 2025, DOI: 10.5517/ccdc.csd.cc2p9y98; (*i*) CCDC 2482211: Experimental Crystal Structure Determination, 2025, DOI: 10.5517/ccdc.csd.cc2p9yb9; (*j*) CCDC 2482212: Experimental Crystal Structure Determination, 2025, DOI: 10.5517/ccdc.csd.cc2p9ycb.

